Energy & Environmental Science

ROYAL SOCIETY OF CHEMISTRY

PAPER

View Article Online
View Journal

Cite this: DOI: 10.1039/d5ee00031a

"Head surgery" of polycyclic *o*-quinones with cyanated aromatic rings towards high electron mobility acceptors enables 19.6% efficiency in additive-free binary organic solar cells†

Tainan Duan, ‡[ae] Jia Wang,‡[b] Xiaochan Zuo,‡[c] Yanyi Zhong,[d] Yuhong Long,[a] Peiran Wang,[b] Kaihuai Tu,[e] Cheng Zhong,[f] Jiangbin Zhang,[d] Oleg A. Rakitin,[g] Zhaoyang Yao,[a] Xiangjian Wan,[a] Yan Zhao,*[c] Bin Kan*[b] and Yongsheng Chen*[a]

Received 2nd January 2025,
Accepted 7th March 2025

DOI: 10.1039/d5ee00031a

rsc.li/ees

The development of high-performance organic electron acceptors is pivotal for advancing organic optoelectronic devices. In this paper, a new synthetic approach was developed to construct fused-ring aromatic backbones and the corresponding electron acceptors, namely **CD-1** and **CD-2**, through an *o*-quinone-mediated cycloaromatization strategy. Both **CD-1** and **CD-2** exhibit a compact 3D interpenetrating network structure with high packing coefficient in a single crystal. Consequently, these newly designed acceptors demonstrate remarkable electron transport capability as evidenced from the high electron mobility over 1.1 $cm^2 V^{-1} s^{-1}$ of **CD-2** based organic field-effect transistor devices. Notably, the additive-free binary organic photovoltaic devices incorporating **CD-1** exhibit power conversion efficiencies (PCEs) of 19.6% with well-balanced open-circuit voltage and short-circuit current density, and the corresponding additive-free binary devices based on **CD-2** achieve a decent PCE of 19.1% as well. These results not only underline the potential of the new molecular design strategy in providing a robust platform for developing high-performance electron acceptors, but also offer valuable insights into the new design guidelines for achieving high efficiency in organic optoelectronic devices.

Broader context

The development of high-performance electron acceptors for organic solar cells (OSCs) hinges on the strategic design and modification of central core units within the molecular structures. These modifications not only influence the electronic properties but also play a pivotal role in controlling the aggregation behavior and overall device performance. However, methods for introducing and modifying central core units remain highly limited. In this work, we introduce a novel approach by incorporating cyano-substituted aromatic rings onto a fused-ring core, realizing two new electron acceptors, **CD-1** and **CD-2**. Both compounds exhibit a three-dimensional packing mode in single crystals, but **CD-1** presents a twisted conformation with moderate packing density, while **CD-2** adopts a planar structure with a high packing density. Consequently, both **CD-1** and **CD-2** show excellent performance in opto-electronic devices: **CD-1**-based binary additive-free OSC devices achieve a power conversion efficiency (PCE) of 19.6%, along with good storage stability; meanwhile, **CD-2** exhibits outstanding electron mobility in OFET devices, with a record mobility of 1.1 $cm^2 V^{-1} s^{-1}$. These findings present a novel strategy for the development of high-performance electron acceptors with significant implications for both molecular innovations and device applications.

[a] *State Key Laboratory and Institute of Elemento-Organic Chemistry, The Centre of Nanoscale Science and Technology and Key Laboratory of Functional Polymer Materials, Renewable Energy Conversion and Storage Center (RECAST), Frontiers Science Center for New Organic Matter, College of Chemistry, Nankai University, Tianjin, 300071, China. E-mail: yschen99@nankai.edu.cn*

[b] *School of Materials Science and Engineering, National Institute for Advanced Materials, Nankai University, Tianjin, 300350, China. E-mail: kanbin04@nankai.edu.cn*

[c] *Laboratory of Molecular Materials and Devices, Department of Materials Science, Fudan University, Shanghai 200433, China. E-mail: zhaoy@fudan.edu.cn*

[d] *Nanhu Laser Laboratory, National University of Defense Technology, Changsha, China and Hunan Provincial Key Laboratory of High Energy Laser Technology, National University of Defense Technology, Changsha, China*

[e] *Chongqing Institute of Green and Intelligent Technology, Chinese Academy of Sciences, Chongqing, 400714, China*

[f] *College of Chemistry and Molecular Sciences, Wuhan University, Wuhan, 430072, China*

[g] *N. D. Zelinsky Institute of Organic Chemistry Russian Academy of Sciences, 47 Leninsky Prospekt, Moscow, Russia*

† Electronic supplementary information (ESI) available. CCDC 2385866 (**CD-1**) and 2385867 (**CD-2**). For ESI and crystallographic data in CIF or other electronic format see DOI: https://doi.org/10.1039/d5ee00031a

‡ These authors contributed equally.

Introduction

Organic solar cells (OSCs) have garnered significant attention due to their high accessibility (solution processing, large-area roll-to-roll printing, *etc.*), flexibility, and adjustable transparency.[1–11] In recent years, the advent of Y-series non-fullerene acceptors (NFAs) has marked a breakthrough in OSC technology.[12–28] Structurally featured with an electron-deficient unit embedded polycyclic central core and two additional electron-deficient terminal groups, these NFAs have led to a notable increase in power conversion efficiencies (PCEs) of OSCs. With the aid of Y-series NFAs, state-of-the-art polymer donor/NFA binary systems have achieved PCEs approaching 20% in single-junction OSCs.[29–41] Attributed to their panchromatic absorption spectra, excellent near-infrared (NIR) emission efficiency, and outstanding electron mobility, Y-series acceptors have not only achieved success in OSCs, but are also gradually making their mark in organic field-effect transistors (OFETs), and phototheranostic agents.[42–46]

Compared to the ITIC- and F-series NFAs, the most significant modification in the molecular design of the Y-series NFAs lies in the introduction of central units (benzothiadiazole, benzotriazole, *etc.*) in the fused ring core that forges a biaxially extended π-conjugated backbone.[47,48] Taking the benzothiadiazole unit as an example, its incorporation not only broadens the absorption spectrum of the acceptor molecule and optimizes energy levels by enhancing intramolecular charge transfer and quinoid character, but more importantly, it also induces the generation of multiple new intermolecular packing modes (''end-to-core'' mode, ''dual end to bridge'' mode, ''central to central'' mode'', *etc.*) other than the traditional ''end-to-end'' mode. Such diverse packing patterns enable the intermolecular packing of acceptors to forge a compact three-dimensional (3D) network, which not only facilitates charge extraction and transport, but also enhances molecular packing density, reduces exciton–phonon coupling, and thereby minimizes the energy loss (E_{loss}) of corresponding OSC devices.[49–51] The indispensable role of the central unit in high-performance acceptors has been further corroborated by recent studies on C-shaped acceptors. Although these thiadiazole-unit-free molecules can achieve a PCE over 18%, their performance still falls significantly short of excellence.[52,53]

Consequently, modifications and functionalization of the central unit have become a research focus in recent years, as researchers aim to further enhance the performance of non-fullerene acceptors. By utilizing a reduction reaction, Zhu *et al.* converted the thiadiazole-embedded backbone of Y-series acceptors to an *ortho*-diamine, which can then undergo condensation/cyclization reactions with *ortho*-quinones or *ortho*-diketones to synthesize new fused-ring cores with more extended central units.[54,55] Building on this, our group oxidized the fused-ring diamine to obtain a more reactive *ortho*-diimine, which can directly undergo efficient condensation reactions with certain *ortho*-diamines at room temperature to acquire the desired conjugated units.[49,56–58] Recently, our group expanded the synthetic methodology and structural diversity of these phenazine-based acceptors by hydrolyzing the *ortho*-diimine into a stable and easily scalable fused-ring *ortho*-quinone.[59] The Qx- and CH-series of acceptors developed using the above-mentioned methods have already achieved a PCE approaching 20% in OSC devices, along with effective suppression of energy loss, demonstrating the superiority and promising potential of these centrally extended acceptors.[51,60–64]

In this work, the conceptual and synthetic landscape of centrally extended acceptors was further expanded. A new synthetic approach was developed to construct fused-ring aromatic backbones and the corresponding electron acceptors through an *ortho*-quinone-mediated cycloaromatization strategy. By the insertion of an anthracene or a benzo[*c*]thiophene unit at the polycyclic π-conjugated backbone, two phenazine-free new acceptors (namely **CD-1** and **CD-2**) were synthesized and systematically characterized. Like their excellent predecessors, the single crystal structures of **CD-1** and **CD-2** also exhibit a compact 3D interpenetrating network structure that endows both materials with satisfactory charge transport capability. This is further evidenced by the high electron mobility of solution processed OFET devices fabricated using these two materials. Moreover, after blending with polymer donor D18, **CD-2** based binary OSC devices achieved a PCE of 19.1%, while the **CD-1**, benefiting from its more suitable energy levels and more optimized morphology of blend films, achieved a high efficiency of 19.6% in binary devices without the use of additives. This work not only expands the pathways for the synthesis of non-fullerene acceptors and the diversity of their structures, but also provides new guidelines for the development of organic electron acceptors with high mobility and high photovoltaic performance.

Results and discussion

The synthetic procedure of CD-series acceptors is depicted in Fig. 1 and Scheme S1 (ESI†). As reported in our previous work, the *ortho*-quinone (compound **1**) was prepared by adopting the 3-step ''reduction–oxidation–hydrolysis'' tandem reaction.[59] However, when attempting to perform cycloaromatization reaction using *ortho*-quinone and dicyano intermediates, it was found that widely-used alkali-derived bases (sodium hydride, sodium methoxide, sodium *tert*-butoxide, *etc.*) not only failed to initiate the reaction but also caused decomposition of the *ortho*-quinone under heating conditions. Finally, we discovered that organic base DBU could efficiently and mildly catalyze the cycloaromatization reaction, enabling the successful synthesis of the desired fused-ring cores in high yields. After obtaining the core units, the acetylation and the Knoevenagel condensation reaction were conducted subsequently, and two new acceptors were achieved accordingly. In this new strategy, highly reactive methylene groups replace the previously used amino groups for cycloaromatization reaction with carbonyl groups, thereby constructing a new kind of π-conjugated center core. Therefore, compared to the synthetic routes of Qx- and CH-series acceptors, CD series acceptors no longer include electron-deficient pyrazine

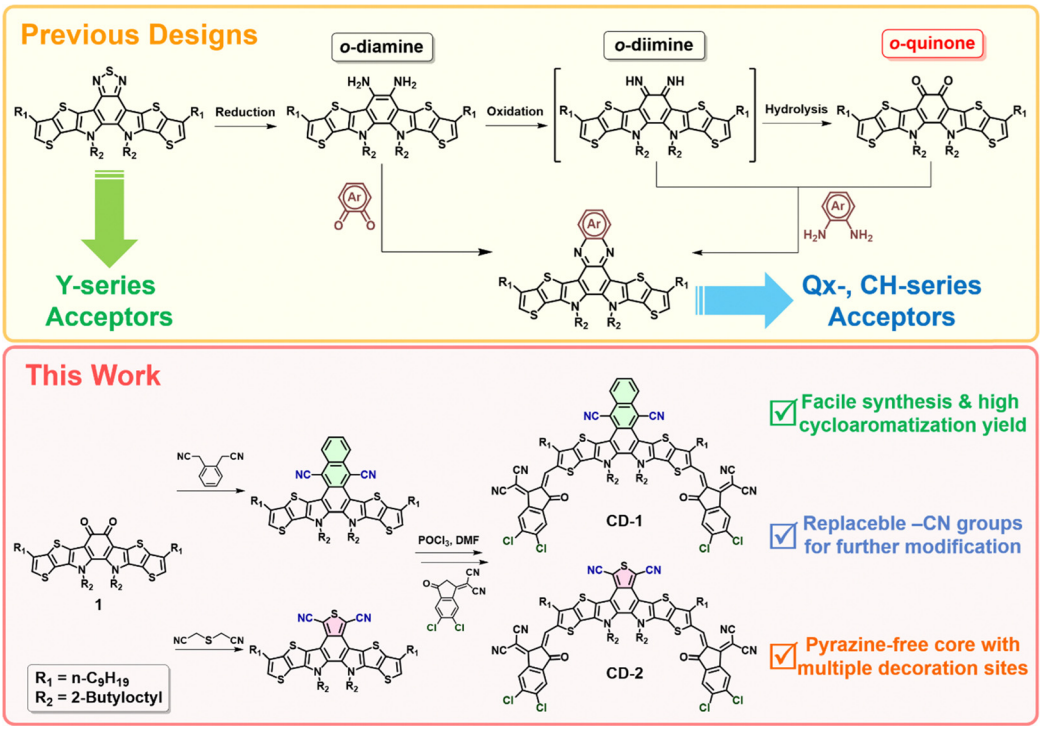

Fig. 1 Molecular designs and synthetic routes of acceptors in previous reports (upper) and in this work (lower).

rings but contain cyano groups that are more readily converted into some other functional groups. Moreover, based on the molecular framework of **CD-1**, further structural modifications can be easily made by introducing substituents onto the terminal benzene ring. This flexibility allows the CD series to complement the Y-series, as well as the Qx- and CH-series acceptors, offering more options for constructing high-performance optoelectronic devices.

Theoretical calculations indicated that the electron density distributions of two molecules revealed a similar polarized manner and typical A–D–A feature, in which the highest occupied molecular orbital (HOMO) is mainly located on the central core while the lowest unoccupied molecular orbital (LUMO) is mainly located on the end groups (Fig. S1–S3, ESI†).[7]

For preliminary characterization of new acceptors, their electrochemical and photophysical behaviors were characterized by cyclic voltammetry (CV) and UV-Vis spectroscopy, respectively. As shown in Fig. 2(b), compared with **CD-2**, both the HOMO (−5.69 eV *vs.* −5.74 eV) and LUMO energy levels (−3.88 eV *vs.* −3.92 eV) of **CD-1** are slightly up-shifted, yet their bandgaps are very close (1.81 eV *vs.* 1.82 eV). This could be attributed to the more electron-rich and more extended π-conjugated central unit of **CD-1**. The energy levels and band gap data of the acceptor molecules are also highly consistent with their UV-Vis absorption spectra. As shown in Fig. 2(a), Fig. S5 and Table S2 (ESI†), **CD-1** and **CD-2** show a maximum absorption peak located at 733 nm and 729 nm in dilute chloroform solution, while in thin films, the peaks red-shifted to 806 nm and 808 nm, respectively, with almost identical absorption onsets (886 nm) and optical band gaps (1.40 eV). It is noteworthy that a large redshift ($\Delta\lambda$) of 79 nm has been observed when transforming from solution to film for **CD-2** which is higher that of **CD-1** (73 nm), suggesting the more compact intermolecular π–π stacking of **CD-2**. The more compact π–π stacking in **CD-2** enhances electronic coupling between adjacent molecules, which leads to a delocalization of π-electrons across the stacked molecules, effectively lowering the energy gap between the HOMO and the LUMO energy levels. As a result, the transition from the ground state to the excited state requires less energy, which manifests as a red-shift in the absorption spectrum. This hypothesis was also confirmed by the results of 2D grazing incidence wide-angle X-ray scattering (GIWAXS) experiments. As shown in Fig. 2(d)–(f), both **CD-1** and **CD-2** demonstrated a clear preference for the face-on orientation and evident (010) peak along the out-of-plane (OOP) direction. Moreover, **CD-2** exhibited smaller *d*-spacing (3.77 Å *vs.* 3.82 Å) and full width at half maximum (FWHM) (0.30 $Å^{-1}$ *vs.* 0.58 $Å^{-1}$) than **CD-2**, and consequently gave much higher coherence length (CL) (19.16 Å *vs.* 9.83 Å), indicating the more crystalline character and higher electron transport potential of **CD-2**. The detailed GIWAXS results are summarized in Table S8 (ESI†). In addition, comprehensive transient absorption spectroscopy (TAS) was performed to investigate the exciton diffusion features of two acceptors. Fig. 2(g) and (j) display 2D TA images of **CD-1** and **CD-2** neat films, while Fig. 2(h) and (k) show their corresponding TA spectra at different probe delay times. Positive ΔA signals indicate photoinduced absorption (PIA) from transient species generated upon photoexcitation, whereas negative ΔA signals arise from ground-state bleaching (GSB) or stimulated emission caused by the probe pulse. The PIA band of **CD-1** and **CD-2** singlet excitons appears near 920 nm. Singlet exciton lifetimes are typically determined from neat film TA

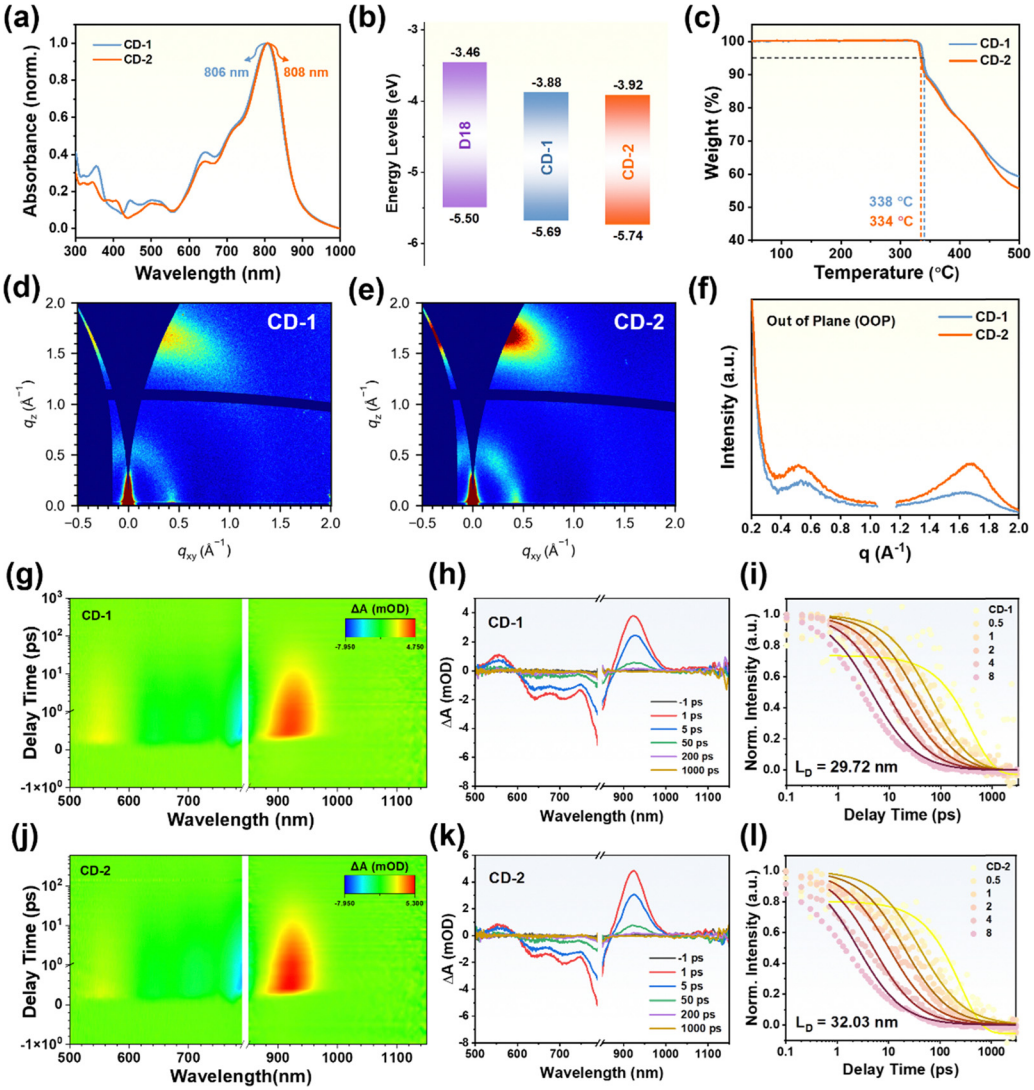

Fig. 2 (a) Normalized thin-film absorption spectra of acceptors. (b) Energy level diagram of D18 and acceptors. (c) TGA curves of acceptors. (d) and (e) 2D GIWAXS patterns and (f) line-cut profiles of neat films. (g) and (j) 2D TAS images and (h) and (k) corresponding TA spectra at different probe delay time of neat films. (i) and (l) Excitation-fluence dependence of the decay kinetics of singlet excitons in neat films.

profiles, ensuring that the decay kinetics of exciton-related signals are independent of excitation fluence.[65–67] Exciton diffusion lengths (L_D) for **CD-1** and **CD-2** were estimated using the exciton–exciton annihilation method *via* pump-fluence-dependent TAS. As shown in Fig. 2(i) and (l), **CD-2** exhibits a prolonged L_D (32.03 nm) compared to **CD-1** (29.72 nm), suggesting faster exciton diffusion and dissociation in **CD-2** compared to that in **CD-1**. In addition, thermogravimetric analysis (TGA) shows that both two acceptor molecules exhibit good thermal stability and decompose (5% loss) only above 330 °C (Fig. 2(c)), which is consistent with previously reported high performance acceptors.

To elucidate the preliminary results from spectroscopic measurements and clarify how the different extended central core affects the packing modes of **CD-1** and **CD-2**, their single crystals were cultivated and analyzed accordingly. The single crystals can be successfully obtained by diffusing methanol vapor into a chloroform solution. The molecular geometry and intermolecular packing pattern (all alkyl chains were omitted for clearer presentation) in a single crystal of **CD-1** (CCDC 2385866†) and **CD-2** (CCDC 2385867†) are displayed in Fig. 3. Similar to most high-performance NFAs, both **CD-1** and **CD-2** exhibit a compact 3D network structure featuring several different intermolecular packing modes in single crystals. However, they show significant differences in molecular conformation and crystal parameters. As shown in Fig. 3(a)–(c), the **CD-1** molecule exhibited a highly twisted, asymmetric molecular conformation, with a dihedral angle of 46.3° between the planes of two end groups, and an even larger dihedral angle of 49.2° between the central unit and end group. This unique twisted conformation might be caused by the steric hindrance from the two cyano groups on the naphthalene central core. Two primary packing modes can be found in the single crystal of **CD-1**, both of which are "dual end-to-bridge" mode, along with a secondary "end-to-end" mode. Despite having twisted

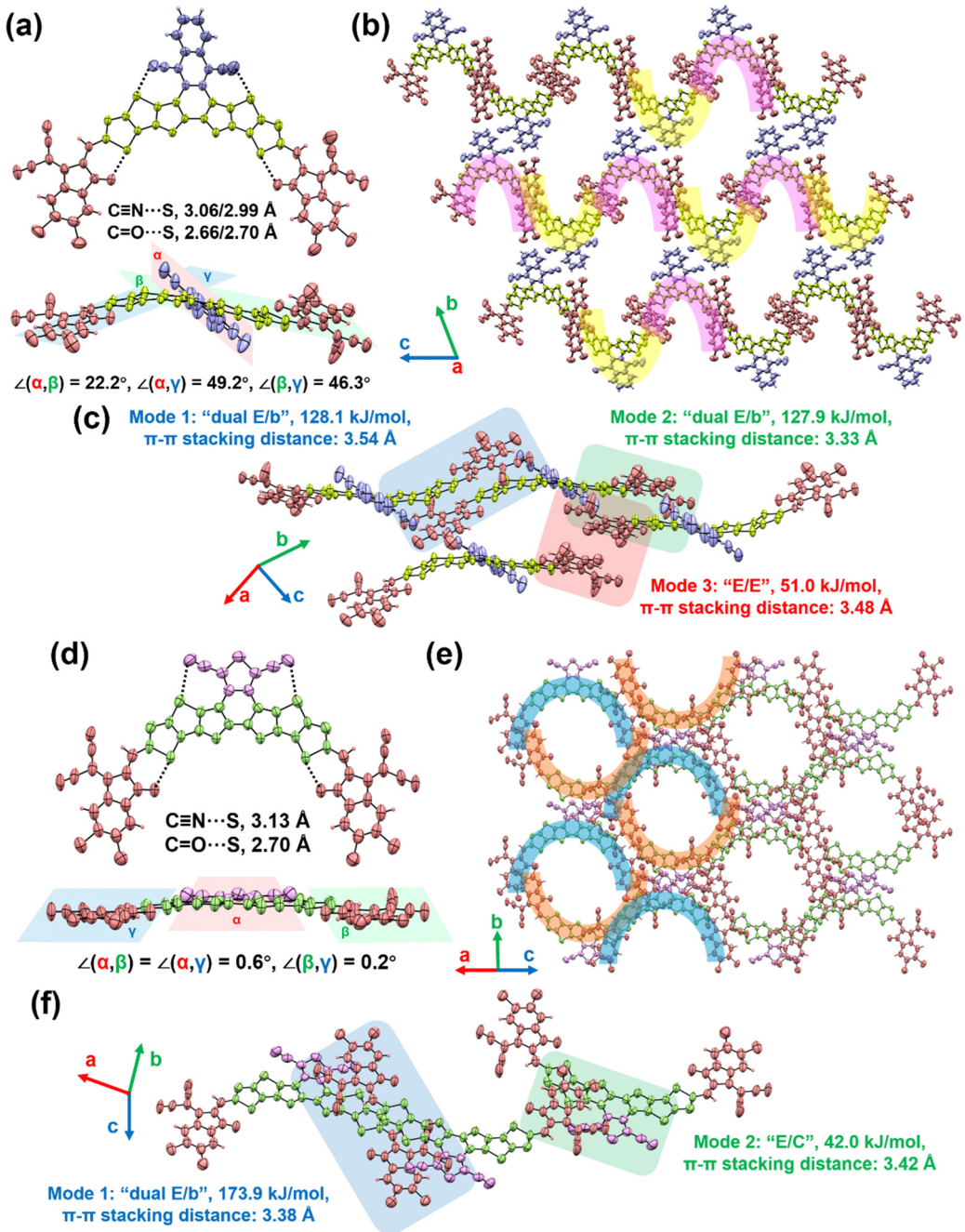

Fig. 3 (a) and (d) Monomolecular single crystallographic structures of **CD-1** and **CD-2** in top- and side-views. The alkyl chains were omitted for clarity. (b) and (e) Illustration of 3D intermolecular packing in **CD-1** and **CD-2**. (c) and (f) Different π–π stacking distances and intermolecular packing potential in **CD-1** and **CD-2**.

molecular conformation, a 3D packing network with relatively low π–π intermolecular stacking distance and high intermolecular potential can still be formed in **CD-1**, as shown in Table 1. In contrast to **CD-1**, the **CD-2** molecule exhibited a highly planar and highly symmetric conformation, with the largest dihedral angle being only 0.6°, resulting from the angle between the planes of two end groups. This is mainly because the five-membered thiophene ring allows the steric hindrance from the cyano groups to be almost negligible. As a result, **CD-2** molecules exhibit only one primary packing mode, also following the "dual end-to-bridge" pattern, along with a secondary "end-to-core" mode. Consequently, the highly planar conformation of **CD-2** greatly reduces the intermolecular distance and significantly enhances the π–π stacking interactions compared with **CD-1**. It is noteworthy that the packing coefficient is 65.6% for **CD-1** (58.9% for **CD-2**), making it one of the most condensed molecular assemblies in NFA molecules.[68,69] These data collected from single crystals are also in perfect

Table 1 Crystallographic and π–π interaction parameters of **CD-1** and **CD-2**

Molecules	Packing mode	$d_{\pi-\pi}$ [a] (Å)	Intermolecular potential (kJ mol^{-1})	Packing coefficient (%)
CD-1	Dual E/b E/E	3.54, 3.33, 3.48	128.1, 127.9, 51.0	58.9[b]/32.7[c]
CD-2	Dual E/b E/C	3.38, 3.42	173.9, 42.0	65.6[b]/35.2[c]

[a] The π–π distance of intermolecular packing modes of **CD-1** and **CD-2**. [b] Packing coefficient of single crystals. [c] Packing coefficient of single crystals with conjugate fragment only.

agreement with the results of UV-Vis absorption and GIWAXS measurements.

The intermolecular packing mode not only affects the physiochemical properties, but also has considerable impact on the intrinsic charge transport properties of acceptors, which is pivotal for achieving high performance optoelectronic devices. To evaluate the capability of charge transport of **CD-1** and **CD-2**, single-crystal OFET devices employing **CD-1** and **CD-2** were fabricated and characterized, respectively. Single crystals of acceptors for devices were obtained *via* a drop-casting method. Fig. 4(a) shows the optical microscopy (azure background) and polarized optical microscopy (black background) image of a **CD-2** single crystal. As can be seen, the rod-like **CD-2** crystal (circled with grey short dash) demonstrates an alternating light (at 0°) and dark (at 45°) with rotation under polarized optical microscopy, indicating the single crystalline characteristics of it.[70–72] Then the single crystal OFETs with a bottom-gate top-contact (BGTC) structure (Fig. 4(b)) were fabricated and placed in a glove box under a nitrogen atmosphere. As shown in Fig. 4(c), both **CD-1** and **CD-2** demonstrated typical unipolar charge transport character. **CD-1** based devices displayed a decent electron mobility (μ_e) of 0.16 cm^2 V^{-1} s^{-1}, and **CD-2** based devices exhibited an essentially improved μ_e of 1.1 cm^2 V^{-1} s^{-1}, which is among the highest records for NFA-based n-type OFET devices.[70–73] The excellent electron transport capability of **CD-2** is not only attributed to its deeper HOMO/LUMO energy levels compared to **CD-1**, but also to its more compact π–π stacking and enhanced intermolecular interactions. Notably, in solution-processed thin-film OFET devices, **CD-2** still exhibited a high μ_e of 0.5 cm^2 V^{-1} s^{-1}, and the mobility of **CD-1** shows only a slight decrease as well (Fig. 4(e) and Fig. S9, ESI†). This undoubtedly contributes to maintaining their satisfactory electron transport capabilities in solution-processed OSC devices.

To evaluate the photovoltaic performance of CD-series acceptors, the OSCs were fabricated and characterized. D18

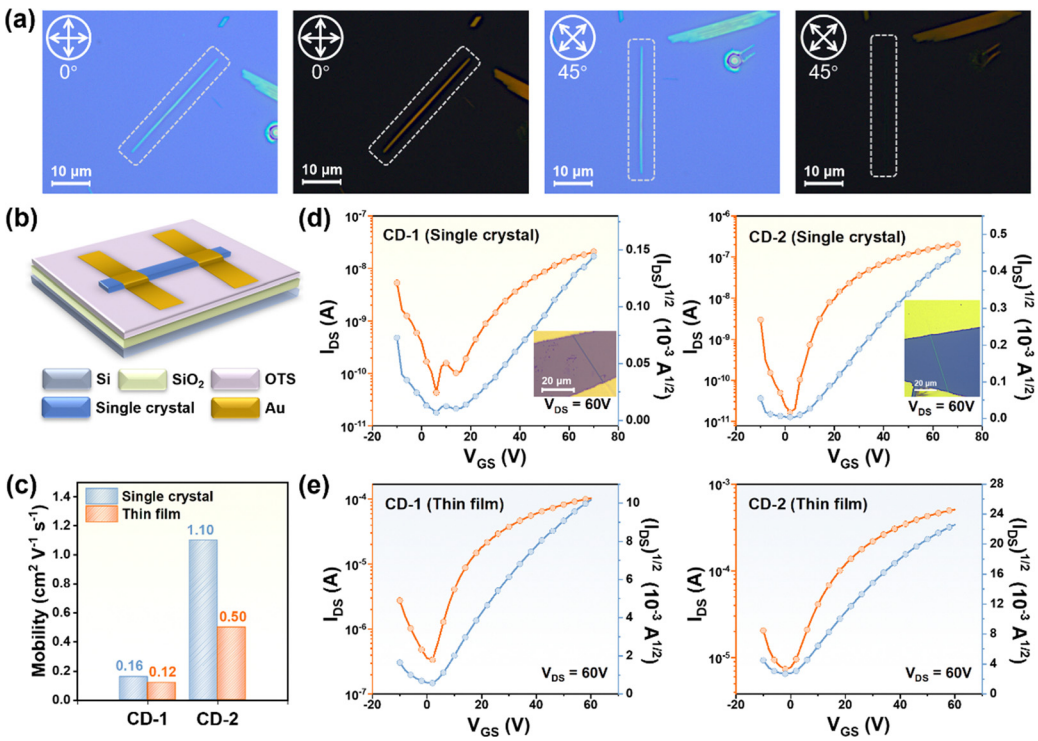

Fig. 4 (a) Optical microscopy and polarized optical microscopy patterns of a single crystal of **CD-2** with rotations of 0° and 45°. (b) Architecture of the single-crystal OFET device. (c) Electron mobility diagram of optimized devices. (d) Transfer curves of OFETs based on the single crystals of **CD-1** and **CD-2**. (e) Transfer curves of OFETs based on the thin films of **CD-1** and **CD-2**.

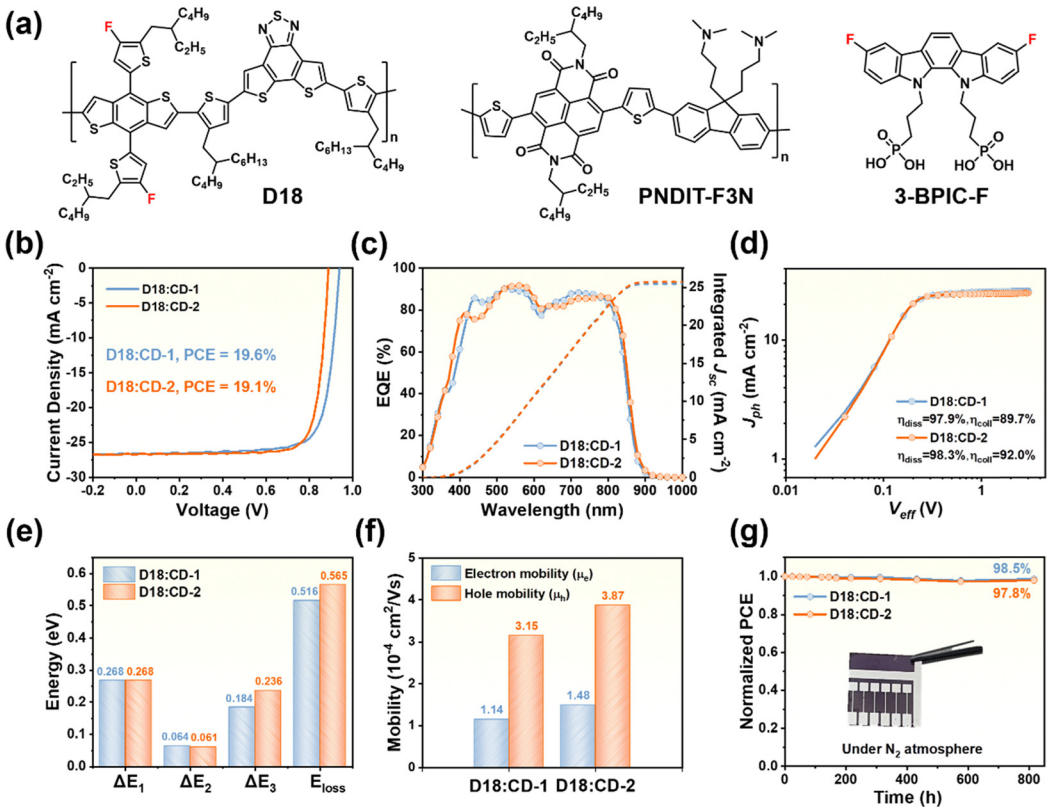

Fig. 5 (a) The organic materials used to fabricate the **CD-1** and **CD-2** based binary OSC devices. (b) Current density–voltage (J–V) characteristics, (c) external quantum efficiency curves, (d) exciton dissociation/charge collection efficiencies, (e) carrier mobility diagram, (f) E_{loss} diagram and (g) shelf stability measurement results of the optimized devices.

was used as a polymer donor and a conventional device architecture of ITO/3-BPIC-F/active blend/PNDIT-F3N/Ag was adopted.[74] The measurement of OSC devices was conducted under simulated solar illumination of AM 1.5G in a nitrogen-filled glovebox. The D18:**CD-1** based binary OSCs afforded three well-balanced parameters, an open-circuit voltage (V_{OC}) of 0.94 V, a short-circuit current density (J_{SC}) of 26.54 mA cm^{-2} and a fill factor (FF) of 78.4%, and consequently a high PCE of 19.6%. Meanwhile, the binary device based on D18:**CD-2** exhibited a slightly higher J_{SC} of 26.74 mA cm^{-2} and an FF up to 80.1% (Fig. 5(b), (c) and Table 2). However, due to a significantly reduced V_{OC} of 0.889 V, the D18:**CD-2** binary device showed only a PCE of 19.1%. It is noteworthy that the optimal PCE for both binary systems can be achieved through simple thermal annealing post-treatment without using any additive, which not only simplifies the operation process for device fabrication, but also suggests the intrinsic superiority of this new series of acceptors.

Table 2 Photovoltaic performance parameters of optimal devices based on **CD-1** and **CD-2** (D18 as the polymer donor)

BHJs	V_{OC} (V)	J_{SC} (mA cm^{-2})	Calc. J_{SC}[a] (mA cm^{-2})	FF (%)	PCE (%)
D18:**CD-1**	0.940	26.54	25.46	78.4	19.6
D18:**CD-2**	0.889	26.74	25.71	80.3	19.1

[a] Current densities calculated from external quantum efficiency curves.

Judging from the results of charge carrier dynamic characterization, the slightly higher J_{SC} of the D18:**CD-2** binary device might be attributed to its better exciton dissociation (η_{diss}, 98.3%) and charge collection efficiency (η_{coll}, 92%) as compared with the D18:**CD-1** binary device (η_{diss} = 97.9%, η_{coll} = 89.7%) (Fig. 5(d)). A higher η_{coll} usually indicates higher hole/electron mobility (μ_h, μ_e) and more balanced μ_h/μ_e in blend films. Therefore, the hole/electron-transport only diodes were fabricated to evaluate the charge transport properties of blend films. Consistent with the data from OFET devices, D18:**CD-1** blends exhibited hole/electron mobilities of 3.15 × 10^{-4}/1.14 × 10^{-4} cm^2 V^{-1} s^{-1} (μ_h/μ_e ratio of 2.76) while D18:**CD-2** blends showed not only higher hole/electron mobilities (3.87 × 10^{-4}/1.48 × 10^{-4} cm^2 V^{-1} s^{-1}) but also a more balanced μ_h/μ_e ratio (2.61) (Fig. 5(f), Fig. S12 and Table S7, ESI†). Transient photocurrent/photovoltage (TPC/TPV) measurements were also conducted to quantitatively analyse the charge recombination/extraction process in OSC devices. As shown in Fig. S14 (ESI†), D18:**CD-1** based devices demonstrated slower charge extraction (0.64 μs *vs.* 0.52 μs), but longer carrier lifetime (86.18 μs *vs.* 46.01 μs) than that of D18:**CD-2** based devices.

It is evident that the main reason the D18:**CD-1** binary device outperforms the D18:**CD-2** device in efficiency is its higher V_{OC}, which is not only related to the higher LUMO energy level of **CD-1** but is also attributed to the alleviated E_{loss} in the D18:**CD-1** binary system. Therefore, a quantitative analysis of the

E_{loss} composition for both binary systems was conducted. The total E_{loss} of both the systems was analyzed and determined using the following equation:

$$E_{loss} = E_g^{PV} - qV_{OC} = (E_g^{PV} - qV_{OC}^{SQ}) + (qV_{OC}^{SQ} - qV_{OC}^{rad}) + (qV_{OC}^{rad} - qV_{OC}) = \Delta E_1 + \Delta E_2 + \Delta E_3$$

The E_g^{PV} represents the bandgap of the blend film which was estimated *via* the derivatives of the sensitive EQE (EQE_{PV}) spectra and q stands for the elementary charge. ΔE_1 represents the unavoidable radiative loss originating from absorption above the bandgap and the V_{OC}^{SQ} is the maximum voltage based on the Shockley–Queisser (SQ) limit; ΔE_2 can be regarded as the radiative energy loss caused by absorption below the bandgap and the V_{OC}^{rad} is the V_{OC} when there is only radiative recombination; ΔE_3 represents the nonradiative recombination energy loss, which is the part that researchers mainly focus on and strive to reduce. As shown in Fig. 5(e) and Table S6 (ESI†), the structural difference of the central unit has negligible impact on ΔE_1 and ΔE_2. However, there is a significant difference between the two binary systems in terms of ΔE_3. As plotted in Fig. S10 (ESI†), a EQE_{EL} record of 2.52×10^{-4} was yielded by the D18:**CD-1** binary device which leads to a low ΔE_3 of 0.184 eV, while the D18:**CD-2** binary device exhibited a much larger ΔE_3 of 0.236 due to its lower EQE_{EL} of 0.348×10^{-4}. Finally, the total E_{loss} was quantified as 0.516 and 0.565 eV for D18:**CD-1** and D18:**CD-2** based binary devices, respectively (Fig. 5(e)). Besides, given the great importance of device lifespan, the stability of two optimized binary devices was preliminarily evaluated. After being stored for 800 hours under a nitrogen atmosphere, the unencapsulated devices can still maintain 98.5% and 97.8% of their initial efficiency for the D18:**CD-1** and D18:**CD-2** binary systems, respectively (Fig. 5(g)). Moreover, the PCEs of D18:**CD-1** and D18:**CD-2** based devices maintained 75% and 71% of their original PCEs after 200 hours of light aging under max power point (MPP) tracking in a nitrogen-filled glovebox (Fig. S8, ESI†), respectively.

Considering that a suitable film morphology and phase separation play crucial roles in achieving favorable charge carrier dynamics and record PCEs in OSCs, the molecular packing behaviors in blend films were investigated using the GIWAXS technique as well. As displayed in Fig. 6(e), (f) and Table S8 (ESI†), both blend films exhibited an obvious (010) peak along the OOP direction around 1.70 $Å^{-1}$, suggesting a face-on orientation that facilitates the charge transport. Compared with D18:**CD-1**, D18:**CD-2** blends exhibit slightly shorter *d*-spacing (3.68 Å *vs.* 3.72 Å) and larger coherence length (CL) along the OOP direction, which would facilitate the charge extraction/transport and boost the FF and J_{SC} of corresponding devices (Fig. 6(g)). These results coincide well with the GIWAXS results of neat films, as well as the enhanced charge carrier mobilities and the improved charge collection efficiencies of the D18:**CD-2** binary device. Atomic force microscopy-based infrared spectroscopy (AFM-IR) was further used to extract

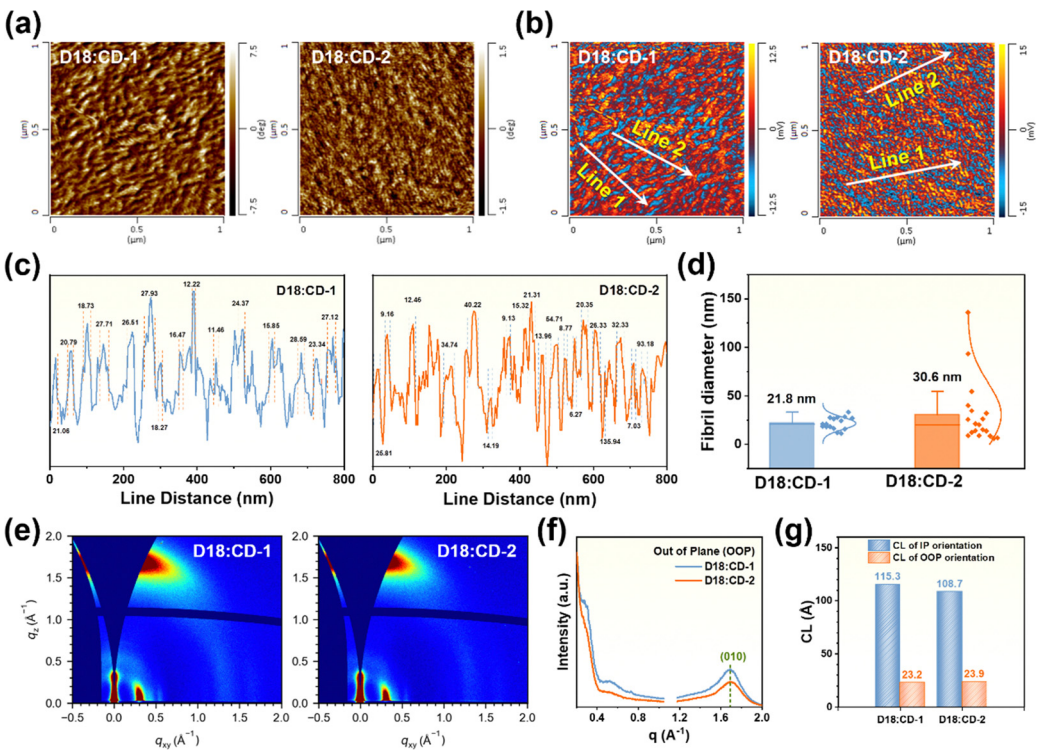

Fig. 6 Morphology characterization of relevant blend films. (a) and (b) Tapping AFM-IR image at the wavenumber of 2216 cm^{-1} of the optimized binary blends. (c) and (d) Line profiles to obtain the fibril width for blended films. The fibril width is estimated from the full-width at half-maximum (the distance between two adjacent dashed lines in the graph). (e) 2D GIWAXS patterns and (f) out of plane line-cut profiles of blend films. (g) Coherence length diagram for the binary blends.

more information from the fibril structure in two binary blends, using the specific IR absorption at 2216 cm^{-1} for **CD-1** and **CD-2** (Fig. S5, ESI†). As shown in Fig. 6(a) and (b), an interpenetrating fibril network can be observed in both binary blend films, which provides sufficient donor/acceptor interfaces and bi-continuous channels for efficient electron/hole transport, consequently leading to the high FF and J_{SC}. This is not only related to the good electron mobility of the **CD-1** and **CD-2**, but also attributed to the suitable miscibility between them and the polymer donor D18 (Fig. S16 and Table S9, ESI†). In addition, the ordered fiber directions were selected for fiber diameter analysis; line profiles across the AFM-IR images are presented in Fig. 6(c) and (d), where the full-width at half-maximum of the peaks was used to estimate the fibril diameter. The average fibril diameters of D18:**CD-1** and D18:**CD-2** were 21.8 and 30.6 nm, respectively. These results are consistent with the exciton diffusion length of the acceptor measured by TAS, and the fiber diameter smaller than the exciton diffusion length is more conducive to the efficient migration of excitons to the donor/acceptor interfaces for charge separation.

Conclusions

In summary, through utilizing our previously reported polycyclic *ortho*-quinones for a cycloaromatization reaction, a new series of electron acceptors with centrally extended π-conjugated backbones were developed. The single-crystal analysis results revealed that both **CD-1** and **CD-2** exhibit a compact 3D interpenetrating network structure with a high packing coefficient, which guarantee their satisfactory charge transport capabilities. Owing to its higher packing coefficient and deeper LUMO energy level, **CD-2** demonstrated electron mobilities of 1.1 $cm^2 V^{-1} s^{-1}$ and 0.5 $cm^2 V^{-1} s^{-1}$ in single-crystal and thin-film OFET devices, respectively, both of which are among the highest values for NFA based devices. However, in OSC devices, **CD-1** achieved a 19.6% efficiency in binary devices due to its higher LUMO energy level and the favorable morphology when blended with polymer donor D18, which is also one of the highest records for additive-free devices. Our work reveals a novel route for the design and synthesis of high-performance electron acceptors, re-emphasizing the importance of extended central units while offering more possibilities for the structural optimization and modification of such acceptors.

Author contributions

T. Duan, B. Kan and Y. Chen designed the work plan for this research. T. Duan, Y. Long, P. Wang and O. A. Rakitin contributed to the materials design and synthesis. T. Duan, P. Wang and K. Tu performed UV-Vis, CV, TGA, DSC and contact angle measurements. Y. Zhong and J. Zhang conducted TAS measurements and data analysis. X. Zuo and Y. Zhao fabricated, optimized the OFET devices, performed relevant characterization and data analysis. J. Wang fabricated and optimized the OSC devices, performed relevant characterization and data analysis. J. Wang also performed the morphology characterization and analysis. C. Zhong conducted the DFT calculation and data analysis. T. Duan wrote the draft manuscript, and all the authors contributed to the revision of the manuscript. Y. Zhao, B. Kan and Y. Chen mentored the other authors throughout the whole research.

Data availability

Data supporting the findings of this study are available within the paper and its ESI.† The crystallographic data in this paper have been deposited at the Cambridge Crystallographic Data Center (CCDC) under accession numbers CCDC 2385866 and 2385867. All other underlying data are available from the corresponding authors upon reasonable request.

Conflicts of interest

The authors declare no conflicts of interest.

Acknowledgements

The authors gratefully acknowledge the financial support from the Ministry of Science and Technology of the People's Republic of China (2023YFE0210400), the National Natural Science Foundation of China (22361132530, 52303237, 52025033, and 52473297), and the Natural Science Foundation of Chongqing (CSTB2023NSCQMSX0268). Oleg A. R. gratefully acknowledges financial support from the Russian Science Foundation (grant no. 24-43-00022). T. Duan thanks Shiyanjia Lab (**https://www.shiyanjia.com**) for providing invaluable assistance with the single crystal analysis.

References

1 K. Leo, *Nat. Rev. Mater.*, 2016, **1**, 16056.
2 H. Yao, L. Ye, H. Zhang, S. Li, S. Zhang and J. Hou, *Chem. Rev.*, 2016, **116**, 7397–7457.
3 L. Meng, Y. Zhang, X. Wan, C. Li, X. Zhang, Y. Wang, X. Ke, Z. Xiao, L. Ding, R. Xia, H.-L. Yip, Y. Cao and Y. Chen, *Science*, 2018, **361**, 1094–1098.
4 C. Yan, S. Barlow, Z. Wang, H. Yan, A. K. Y. Jen, S. R. Marder and X. Zhan, *Nat. Rev. Mater.*, 2018, **3**, 18003.
5 G. Zhang, J. Zhao, P. C. Y. Chow, K. Jiang, J. Zhang, Z. Zhu, J. Zhang, F. Huang and H. Yan, *Chem. Rev.*, 2018, **118**, 3447–3507.
6 S. Liu, J. Yuan, W. Deng, M. Luo, Y. Xie, Q. Liang, Y. Zou, Z. He, H. Wu and Y. Cao, *Nat. Photonics*, 2020, **14**, 300–305.
7 X. Wan, C. Li, M. Zhang and Y. Chen, *Chem. Soc. Rev.*, 2020, **49**, 2828–2842.
8 H. Chen, R. Zhang, X. Chen, G. Zeng, L. Kobera, S. Abbrent, B. Zhang, W. Chen, G. Xu, J. Oh, S.-H. Kang, S. Chen, C. Yang, J. Brus, J. Hou, F. Gao, Y. Li and Y. Li, *Nat. Energy*, 2021, **6**, 1045–1053.

9 G. Zhang, F. R. Lin, F. Qi, T. Heumueller, A. Distler, H.-J. Egelhaaf, N. Li, P. C. Y. Chow, C. J. Brabec, A. K. Y. Jen and H.-L. Yip, *Chem. Rev.*, 2022, **122**, 14180–14274.
10 L. Zhu, M. Zhang, J. Xu, C. Li, J. Yan, G. Zhou, W. Zhong, T. Hao, J. Song, X. Xue, Z. Zhou, R. Zeng, H. Zhu, C.-C. Chen, R. C. I. MacKenzie, Y. Zou, J. Nelson, Y. Zhang, Y. Sun and F. Liu, *Nat. Mater.*, 2022, **21**, 656–663.
11 J. Yi, G. Zhang, H. Yu and H. Yan, *Nat. Rev. Mater.*, 2024, **9**, 46–62.
12 J. Yuan, Y. Zhang, L. Zhou, G. Zhang, H.-L. Yip, T.-K. Lau, X. Lu, C. Zhu, H. Peng, P. A. Johnson, M. Leclerc, Y. Cao, J. Ulanski, Y. Li and Y. Zou, *Joule*, 2019, **3**, 1140–1151.
13 Z. Jia, Q. Ma, Z. Chen, L. Meng, N. Jain, I. Angunawela, S. Qin, X. Kong, X. Li, Y. Yang, H. Zhu, H. Ade, F. Gao and Y. Li, *Nat. Commun.*, 2023, **14**, 1236.
14 H. Lu, W. Liu, G. Ran, Z. Liang, H. Li, N. Wei, H. Wu, Z. Ma, Y. Liu, W. Zhang, X. Xu and Z. Bo, *Angew. Chem., Int. Ed.*, 2023, **62**, e202314420.
15 S. Luo, C. Li, J. Zhang, X. Zou, H. Zhao, K. Ding, H. Huang, J. Song, J. Yi, H. Yu, K. S. Wong, G. Zhang, H. Ade, W. Ma, H. Hu, Y. Sun and H. Yan, *Nat. Commun.*, 2023, **14**, 6964.
16 M. An, Q. Liu, S. Y. Jeong, B. Liu, E. Huang, Q. Liang, H. Li, G. Zhang, H. Y. Woo, L. Niu, X. Guo and H. Sun, *Angew. Chem., Int. Ed.*, 2024, **63**, e202410498.
17 Z. Chen, Y. Xiao, H. Yao, J. Ren, T. Zhang, J. Qiao, S. Zhu, R. Lin, X. Hao and J. Hou, *Adv. Mater.*, 2024, **36**, 2408858.
18 J. Fu, Q. Yang, P. Huang, S. Chung, K. Cho, Z. Kan, H. Liu, X. Lu, Y. Lang, H. Lai, F. He, P. W. K. Fong, S. Lu, Y. Yang, Z. Xiao and G. Li, *Nat. Commun.*, 2024, **15**, 1830.
19 W. Gao, R. Ma, T. A. Dela Pena, C. Yan, H. Li, M. Li, J. Wu, P. Cheng, C. Zhong, Z. Wei, A. K. Y. Jen and G. Li, *Nat. Commun.*, 2024, **15**, 1946.
20 D. Hu, H. Tang, C. Chen, D.-J. Lee, S. Lu, G. Li, H.-Y. Hsu and F. Laquai, *Adv. Mater.*, 2024, 2406949.
21 J. Huang, T. Chen, L. Mei, M. Wang, Y. Zhu, J. Cui, Y. Ouyang, Y. Pan, Z. Bi, W. Ma, Z. Ma, H. Zhu, C. Zhang, X.-K. Chen, H. Chen and L. Zuo, *Nat. Commun.*, 2024, **15**, 3287.
22 C. Li, G. Yao, X. Gu, J. Lv, Y. Hou, Q. Lin, N. Yu, M. S. Abbasi, X. Zhang, J. Zhang, Z. Tang, Q. Peng, C. Zhang, Y. Cai and H. Huang, *Nat. Commun.*, 2024, **15**, 8872.
23 Y. Li, Z. Ge, L. Mei, H. Ma, Y. Chen, X. Wang, J. Yu, G. Lu, R. Yang, X.-K. Chen, S. Yin and Y. Sun, *Angew. Chem., Int. Ed.*, 2024, **63**, e202411044.
24 Z. Luo, W. Wei, R. Ma, G. Ran, M. H. Jee, Z. Chen, Y. Li, W. Zhang, H. Y. Woo and C. Yang, *Adv. Mater.*, 2024, **36**, 2407517.
25 X. Song, L. Mei, X. Zhou, H. Li, H. Xu, X. Liu, S. Gao, S. Xu, Y. Yang, W. Zhu, J. Wang, X.-H. Zhang and X.-K. Chen, *Angew. Chem., Int. Ed.*, 2024, **63**, e202411512.
26 C. Wang, X. Ma, D. Deng, H. Zhang, R. Sun, J. Zhang, L. Zhang, M. Wu, J. Min, Z.-G. Zhang and Z. Wei, *Nat. Commun.*, 2024, **15**, 8494.
27 M. Zhang, Z. Wang, L. Zhu, R. Zeng, X. Xue, S. Liu, J. Yan, Z. Yang, W. Zhong, G. Zhou, L. Kan, J. Xu, A. Zhang, J. Deng, Z. Zhou, J. Song, H. Jing, S. Xu, Y. Zhang and F. Liu, *Adv. Mater.*, 2024, 2407297.
28 B. Zou, A. Liang, P. Ding, J. Yao, X. Zeng, H. Li, R. Ma, C. Li, W. Wu, D. Chen, M. Qammar, H. Yu, J. Yi, L. Guo, S. Ho Pun, J. E. Halpert, G. Li, Z. Kan and H. Yan, *Angew. Chem., Int. Ed.*, 2024, e202415332.
29 Y. Liang, D. Zhang, Z. Wu, T. Jia, L. Luer, H. Tang, L. Hong, J. Zhang, K. Zhang, C. J. Brabec, N. Li and F. Huang, *Nat. Energy*, 2022, **7**, 1180–1190.
30 R. Sun, T. Wang, X. Yang, Y. Wu, Y. Wang, Q. Wu, M. Zhang, C. J. Brabec, Y. Li and J. Min, *Nat. Energy*, 2022, **7**, 1087–1099.
31 J. Wang, P. Xue, Y. Jiang, Y. Huo and X. Zhan, *Nat. Rev. Chem.*, 2022, **6**, 614–634.
32 C. Chen, L. Wang, W. Xia, K. Qiu, C. Guo, Z. Gan, J. Zhou, Y. Sun, D. Liu, W. Li and T. Wang, *Nat. Commun.*, 2024, **15**, 6865.
33 P. Ding, Z. Chen, D. Yang, X. Yu, J. Shi, Y. Chen, J. Zhu, J. Wu, X. Cao, L. Xie, F. Chen and Z. Ge, *Adv. Mater.*, 2024, 2414080.
34 Z. Fu, J.-W. Qiao, F.-Z. Cui, R.-H. Gui, P. Lu, H. Yin, X.-Y. Du and X.-T. Hao, *Adv. Mater.*, 2024, 2413317.
35 Y. Jiang, S. Sun, R. Xu, F. Liu, X. Miao, G. Ran, K. Liu, Y. Yi, W. Zhang and X. Zhu, *Nat. Energy*, 2024, **9**, 975–986.
36 Y. Lang, H. Lai, Y. Fu, R. Ma, P. W. K. Fong, H. Li, K. Liu, X. Yang, X. Lu, T. Yang, G. Li and F. He, *Adv. Mater.*, 2024, 2413270.
37 C. Liao, X. Xu, T. Yang, W. Qiu, Y. Duan, R. Li, L. Yu and Q. Peng, *Adv. Mater.*, 2024, **36**, 2411071.
38 Y. Sun, L. Wang, C. Guo, J. Xiao, C. Liu, C. Chen, W. Xia, Z. Gan, J. Cheng, J. Zhou, Z. Chen, J. Zhou, D. Liu, T. Wang and W. Li, *J. Am. Chem. Soc.*, 2024, **146**, 12011–12019.
39 L. Wang, C. Chen, Y. Fu, C. Guo, D. Li, J. Cheng, W. Sun, Z. Gan, Y. Sun, B. Zhou, C. Liu, D. Liu, W. Li and T. Wang, *Nat. Energy*, 2024, **9**, 208–218.
40 Y. Wang, K. Sun, C. Li, C. Zhao, C. Gao, L. Zhu, Q. Bai, C. Xie, P. You, J. Lv, X. Sun, H. Hu, Z. Wang, H. Hu, Z. Tang, B. He, M. Qiu, S. Li and G. Zhang, *Adv. Mater.*, 2024, **36**, 2411957.
41 R. Zhang, H. Chen, T. Wang, L. Kobera, L. He, Y. Huang, J. Ding, B. Zhang, A. Khasbaatar, S. Nanayakkara, J. Zheng, W. Chen, Y. Diao, S. Abbrent, J. Brus, A. H. Coffey, C. Zhu, H. Liu, X. Lu, Q. Jiang, V. Coropceanu, J.-L. Bredas, Y. Li, Y. Li and F. Gao, *Nat. Energy*, 2025, **10**, 124–134.
42 Y. Gu, H. Lai, Z.-Y. Chen, Y. Zhu, Z. Sun, X. Lai, H. Wang, Z. Wei, L. Chen, L. Huang, Y. Zhang, F. He and L. Tian, *Angew. Chem., Int. Ed.*, 2023, **62**, e202303476.
43 C. Li, G. Jiang, J. Yu, W. Ji, L. Liu, P. Zhang, J. Du, C. Zhan, J. Wang and B. Z. Tang, *Adv. Mater.*, 2023, **35**, 2208229.
44 X. Gu, Y. Wei, R. Zeng, J. Lv, Y. Hou, N. Yu, S. Tan, Z. Wang, C. Li, Z. Tang, Q. Peng, F. Liu, Y. Cai, X. Zhang and H. Huang, *Angew. Chem., Int. Ed.*, 2024, e202418926.
45 G. Niu, X. Bi, Y. Kang, H. Zhao, R. Li, M. Ding, B. Zhou, Y. Zhai, X. Ji and Y. Chen, *Adv. Mater.*, 2024, **36**, 2407199.
46 J. Xia, S. Xie, Y. Huang, X.-X. Wu and B. Lu, *Chem. Commun.*, 2024, **60**, 8526–8536.
47 B. Fan, H. Gao and A. K. Y. Jen, *ACS Nano*, 2023, **18**, 136–154.

48 Z. Yao, X. Wan, C. Li and Y. Chen, *Acc. Mater. Res.*, 2023, **4**, 772–785.
49 H. Chen, Y. Zou, H. Liang, T. He, X. Xu, Y. Zhang, Z. Ma, J. Wang, M. Zhang, Q. Li, C. Li, G. Long, X. Wan, Z. Yao and Y. Chen, *Sci. China: Chem.*, 2022, **65**, 1362–1373.
50 Y. Jiang, Y. Li, F. Liu, W. Wang, W. Su, W. Liu, S. Liu, W. Zhang, J. Hou, S. Xu, Y. Yi and X. Zhu, *Nat. Commun.*, 2023, **14**, 5079.
51 K. Liu, Y. Jiang, G. Ran, F. Liu, W. Zhang and X. Zhu, *Joule*, 2024, **8**, 835–851.
52 Y.-J. Xue, Z.-Y. Lai, H.-C. Lu, J.-C. Hong, C.-L. Tsai, C.-L. Huang, K.-H. Huang, C.-F. Lu, Y.-Y. Lai, C.-S. Hsu, J.-M. Lin, J.-W. Chang, S.-Y. Chien, G.-H. Lee, U. S. Jeng and Y.-J. Cheng, *J. Am. Chem. Soc.*, 2023, **146**, 833–848.
53 Y. Gong, T. Zou, X. Li, S. Qin, G. Sun, T. Liang, R. Zhou, J. Zhang, J. Zhang, L. Meng, Z. Wei and Y. Li, *Energy Environ. Sci.*, 2024, **17**, 6844–6855.
54 Z. Zhou, W. Liu, G. Zhou, M. Zhang, D. Qian, J. Zhang, S. Chen, S. Xu, C. Yang, F. Gao, H. Zhu, F. Liu and X. Zhu, *Adv. Mater.*, 2020, **32**, 1906324.
55 Y. Shi, Y. Chang, K. Lu, Z. Chen, J. Zhang, Y. Yan, D. Qiu, Y. Liu, M. A. Adil, W. Ma, X. Hao, L. Zhu and Z. Wei, *Nat. Commun.*, 2022, **13**, 3256.
56 H. Chen, H. Liang, Z. Guo, Y. Zhu, Z. Zhang, Z. Li, X. Cao, H. Wang, W. Feng, Y. Zou, L. Meng, X. Xu, K. Bin, C. Li, Z. Yao, X. Wan, Z. Ma and Y. Chen, *Angew. Chem., Int. Ed.*, 2022, **61**, e202209580.
57 Y. Zou, H. Chen, X. Bi, X. Xu, H. Wang, M. Lin, Z. Ma, M. Zhang, C. Li, X. Wan, G. Long, Y. Zhaoyang and Y. Chen, *Energy Environ. Sci.*, 2022, **15**, 3519–3533.
58 H. Chen, Z. Zhang, P. Wang, Y. Zhang, K. Ma, Y. Lin, T. Duan, T. He, Z. Ma, G. Long, C. Li, B. Kan, Z. Yao, X. Wan and Y. Chen, *Energy Environ. Sci.*, 2023, **16**, 1773–1782.
59 T. Duan, W. Feng, Y. Li, Z. Li, Z. Zhang, H. Liang, H. Chen, C. Zhong, S. Jeong, C. Yang, S. Chen, S. Lu, O. A. Rakitin, C. Li, X. Wan, B. Kan and Y. Chen, *Angew. Chem., Int. Ed.*, 2023, **62**, e202308832.
60 H. Chen, B. Kan, P. Wang, W. Feng, L. Li, S. Zhang, T. Chen, Y. Yang, T. Duan, Z. Yao, C. Li, X. Wan and Y. Chen, *Angew. Chem., Int. Ed.*, 2023, **62**, e202307962.
61 H. Liang, X. Bi, H. Chen, T. He, Y. Lin, Y. Zhang, K. Ma, W. Feng, Z. Ma, G. Long, C. Li, B. Kan, H. Zhang, O. A. Rakitin, X. Wan, Z. Yao and Y. Chen, *Nat. Commun.*, 2023, **14**, 4707.
62 Z. Yao, X. Cao, X. Bi, T. He, Y. Li, X. Jia, H. Liang, Y. Guo, G. Long, B. Kan, C. Li, X. Wan and Y. Chen, *Angew. Chem., Int. Ed.*, 2023, **62**, e202312630.
63 T. Duan, J. Wang, X. Zuo, X. Bi, C. Zhong, Y. Li, Y. Long, K. Tu, W. Zhang, K. Yang, H. Zhou, X. Wan, Y. Zhao, B. Kan and Y. Chen, *Mater. Horiz.*, 2024, **11**, 4413–4423.
64 Z. Zhang, S. Yuan, T. Chen, J. Wang, Y.-Q.-Q. Yi, B. Zhao, M. Li, Z. Yao, C. Li, X. Wan, G. Long, B. Kan and Y. Chen, *Energy Environ. Sci.*, 2024, **17**, 5719–5729.
65 Y. Tamai, *Aggregate*, 2022, **3**, e280.
66 W. Feng, Y. Bai, J. Wang, Y. Zhong, J. Wang, T. Chen, J. Zhang, K. Han, X. Wan, B. Kan and Y. Chen, *Adv. Energy Mater.*, 2024, 2404062.
67 Y. Tamai, Y. Murata, S.-i Natsuda and Y. Sakamoto, *Adv. Energy Mater.*, 2024, **14**, 202301890.
68 C. Li, J. Zhou, J. Song, J. Xu, H. Zhang, X. Zhang, J. Guo, L. Zhu, D. Wei, G. Han, J. Min, Y. Zhang, Z. Xie, Y. Yi, H. Yan, F. Gao, F. Liu and Y. Sun, *Nat. Energy*, 2021, **6**, 605–613.
69 H. Lai, H. Chen, Z.-Y. Chen, Y. Lang, Y. Zhu, S.-T. Zhang, X. Lai, P. Tan, Y. Zhang, B. Yang, G. Li and F. He, *Energy Environ. Sci.*, 2023, **16**, 5944–5955.
70 Y. Chen, Z. Wu, L. Ding, S. Zhang, Z. Chen, W. Li, Y. Zhao, Y. Wang and Y. Liu, *Adv. Funct. Mater.*, 2023, **33**, 202304316.
71 Z. Wu, W. Liu, X. Yang, W. Li, L. Zhao, K. Chi, X. Xiao, Y. Yan, W. Zeng, Y. Liu, H. Chen and Y. Zhao, *Angew. Chem., Int. Ed.*, 2023, **62**, e202307695.
72 T. Duan, J. Wang, W. Shi, Y. Li, K. Tu, X. Bi, C. Zhong, J. Lv, K. Yang, Z. Xiao, B. Kan and Y. Zhao, *Angew. Chem., Int. Ed.*, 2024, **63**, e202407890.
73 X. Song, N. Gasparini, M. M. Nahid, H. Chen, S. M. Macphee, W. Zhang, V. Norman, C. Zhu, D. Bryant, H. Ade, I. McCulloch and D. Baran, *Adv. Funct. Mater.*, 2018, **28**, 1802895.
74 H. Liu, Y. Xin, Z. Suo, L. Yang, Y. Zou, X. Cao, Z. Hu, B. Kan, X. Wan, Y. Liu and Y. Chen, *J. Am. Chem. Soc.*, 2024, **146**, 14287–14296.